



OPEN

3-D electromagnetic radiative non-Newtonian nanofluid flow with Joule heating and higher-order reactions in porous materials

Amel A. Alaidrous¹✉ & Mohamed R. Eid^{2,3}✉

The aim of this work is to discuss the effect of m th-order reactions on the magnetic flow of hyperbolic tangent nanofluid through extending surface in a porous material with thermal radiation, several slips, Joule heating, and viscous dissipation. In order to convert non-linear partial differential governing equations into ordinary ones, a technique of similarity transformations has been implemented and then solved using the OHAM (optimal homotopy analytical method). The outcomes of novel effective parameters on the non-dimensional interesting physical quantities are established utilizing the tabular and pictorial outlines. After a comparison with previous literature studies, the results were finely compliant. The study explores that the reduced Nusselt number is diminished for the escalating values of radiation, porosity, and source (sink) parameters. It is found that the order of the chemical reaction $m = 2$ is dominant in concentration as well as mass transfer in both destructive and generative reactions. When m reinforces for a destructive reaction, mass transfer is reduced with 34.7% and is stabled after $\eta = 3$. In the being of the destructive reaction and Joule heating, the nanofluid's temperature is enhanced.

Abbreviations

a, b	Constants (-)
B_0	Magnetic parameter
C	Concentration (mol/m ³)
c_p	Specific heat
C_∞	Free stream concentration (mol/m ³)
C_w	Constant-wall concentration (mol/m ³)
D_B	Brownian diffusion (m ² /s)
D_T	Thermophoresis diffusion (m ² /s)
Ec	Eckert number (-)
f, g	Dimensionless stream functions (-)
f_w	Suction/injection parameter (-)
k	Thermal conductivity (W/mK)
K	Porous medium permeability (-)
K_1	Porous medium parameter (-)
k_c	Chemical reaction (-)
k^*	Mean-absorption factor
Le	Lewis number (-)
M	Magnetic parameter (-)
m	Order of reactions (-)
n	Power-law index (-)

¹Department of Mathematics, Faculty of Applied Sciences, Umm Al-Qura University, Makkah 21955, Saudi Arabia. ²Department of Mathematics, Faculty of Science, New Valley University, Al-Kharga, Al-Wadi Al-Gadid 72511, Egypt. ³Department of Mathematics, Faculty of Science, Northern Border University, Arar 1321, Saudi Arabia. ✉email: dr.amollah_gol@hotmail.com; m_r_eid@yahoo.com

N_b	Brownian motion parameter (-)
N_t	Thermophoresis parameter (-)
N_1, N_2	Coefficients of slip velocity (-)
Q	Heat source (sink) (W/m^2 K)
q_r	Radiative heat flux (W/m^2)
R_d	Thermal ray (-)
S	Heat source (-)
Pr	Prandtl number (-)
T	Temperature (K)
T_w	Constant-wall temperature (K)
T_∞	Free-stream temperature (K)
u, v, w	Velocity components (ms^{-1})
We_x, We_y	Numbers of Weissenberg (-)
w_0	Suction (injection) parameter (-)
x, y, z	Space coordinates (m)

Greek symbols

$\alpha = \frac{k}{\rho c_p}$	Thermal diffusivity ($J/m^3 \cdot K$)
δ_1, δ_2	Velocity slip parameters
γ	Chemical reaction (-)
η	Similarity parameter (-)
θ	Dimensionless temperature
λ	Constant parameter of sheet (-)
μ	Dynamic viscosity (Pa s)
ν	Kinematic viscosity (m^2/s)
ρ	Density (kg/m^3)
$(\rho c_p)_f$	Heat capacity of the base fluid ($J/kg \cdot K$)
$(\rho c_p)_s$	Heat capacity of a nanoparticle ($J/kg \cdot K$)
σ	The electrical conductivity
σ^*	Constant of Stefan-Boltzmann
$\tau = \frac{(\rho c_p)_s}{(\rho c_p)_f}$	Ratio between the heat capacities (-)
ϕ	Dimensionless concentration (-)
Γ	Williamson parameter (-)

Subscripts

∞	Free stream condition
f	Base fluid
s	Solid nanoparticle
w	Wall

Abbreviations

3-D	Three-dimensions
OHAM	Optimal homotopy analytical method
MHD	Magnetohydrodynamics
MRI	Magnetic resonance imaging
PDEs	Partial differential equations
ODEs	Ordinary differential equations

The heat movement for a viscous fluid has many manufacturing, bio-medical and engineering applications like a capacity generator, rock-oil productions, plasma research, cancer treatment, aerodynamics laminar boundary-layer predominance, and many more. But for that place, this idea takes a long journey to shape up. In 1904, Prandtl proposed the idea of laminar boundary-layers that the viscous effect should be confined to thin shear surfaces adjacent to boundaries in the situation of very low-viscosity fluids¹. Sakiadis^{2,3} probed the boundary layer Blasius movement wing to the surface being supplied at relaxation with constant velocity from a slit into a stream. Crane⁴ examined the movement over an extending plate. Many academics for example^{5,6} extended the Crane⁴ work. Various researchers are elaborated on various features of these problems for example⁷⁻¹⁰. Different numerical investigations of heat transfer under various effects of one-phase nanofluids flow are elaborated in¹¹⁻¹⁴. Gholinia et al.¹⁵ analyzed the characterization of the 3-D stagnation point hybrid nanofluid flowing over a circulatory cylinder with sinusoidal length. Numerical aspects of 3-D free convection MHD GO-MoS₂/H₂O-C₂H₆O₂ mixture nanofluid with radiation and slip effects is are debated by Ghadikolaei and Gholinia¹⁶. Whilst the flow of free convection past a surface in a porous medium is checked by Hady et al.^{17,18} of a nanofluid through a cone. They achieved solutions by utilizing MATLAB techniques such as bvp4c or Runge-Kutta method.

In chemistry, manufacturing, energy storage, biomedical application, drug delivery based on temperature-controlled, energy storage and conversion, nanoparticles impact plays a very significant role¹⁹. Ray is used in human forms for drugs, mining, hospital radiology, MRI scans, etc. Heat transfer properties of viscous fluid flow

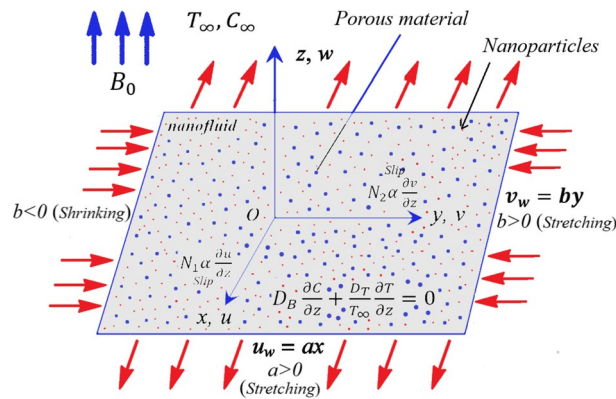


Figure 1. Geometric flow model.

with radiation and nanoparticles via a non-linearly extending surface are elucidated by Hady et al.²⁰. Kumar et al.²¹ described the MHD and chemically reacting effects of 3-D non-Newtonian fluid flow past porous material. Hamid et al.²² analyzed the flow of free convection non-Newtonian Casson fluid in a trapezoidal cavity. Other important studies in the flow of non-Newtonian fluid are found in^{23,24}. Combined impacts of MHD solar radiation, Joule heating, chemical reaction, and viscous dissipation, on the nanofluid flow past a heated expanding plate immersed in a saturated porous matrix, are demonstrated by Eid and Makinde²⁵. Eid et al.²⁶ analysis of magnetic flow through a circular cylinder of SWCNTs based-blood in with non-linear radiation and source (sink) of heat.

In construction, electronics and heat transport process in the emerging biotechnology and nanotechnology manufacture, etc., MHD and chemical reactions play an important role. In MHD there are sundry applications which are astronomy, earthquakes, metal adaptors, etc. In an exponentially expanding surface, Eid²⁷ clarified the issue of the chemically reactive species on and heat source (sink) influences on MHD nanofluid flow via a porous surface. Whilst, the combined impacts of hydro-magnetic and heat source (sink) on unstable convective heat and mass transfer of a power-law nanofluid through a permeable stretch plate are addressed by Eid and Mahny²⁸. Durgaprasad et al.²⁹ Hassan analyzed the 3-D Casson nanofluid flow using the Buongiorno model across a slender surface of a porous regime. Prasad et al.³⁰ screened over a semi-infinite plate with an analytical approximation on MHD flow of nanofluid. Time-dependent Couette flow with heat transfer under the combined effects of thermal radiation and MHD with varying thermo-physical properties are explored numerically for Cu–H₂O nanofluids by Wakif et al.³¹. Over an extending plate with the influences of heat and mass transport on hydro-magnetic nanofluid flow are deliberated by Gholinia et al.³². In this article, they utilized Runge–Kutta scheme to offer graphical exemplification. Heat transfer of a squeezed time-dependent Fe₃O₄–H₂O nanofluid movement among two-parallel surfaces in case of variable thermal conductivity is explored by Lahmar et al.³³ in the influence of the magnetic field.

The irregular tendency of nanofluid in modern days is due to its unforeseen thermal characteristics and has a dynamic part in enhancing the heat transport of material transmutation and manufacturing thermal management. The discussion of the heat transfer features of gold nanoparticles past a power-law extending plate of Sisko flow based-blood with radiation is elaborated by Eid et al.³⁴. The impacts of slip and heat source (sink) on the unsteady heat transfer of a stagnation point nanofluid flow via an extending plate in a porous substance are determined by Eid³⁵. The Marangoni influences on the nanofluid flowing of Casson type in with convective conditions are described by Kumar et al.³⁶. Several investigators intensively reviewed the transfer of heat of nanofluids such as^{37–45}. A variety of scholars have already documented a useful study of the hyperbolic tangent fluid model that preserves various flow phenomena. MHD of convectively heated and condensed tangent hyperbolic nanofluid over an extending surface on the slip flux is showed by Ibrahim⁴⁶. Over an extended surface with the radiative flow of convective tangent hyperbolic liquid is illustrated by Mahanthesh et al.⁴⁷. The issue of tangent-hyperbolic fluid flow past various types of shapes with different impacts of parameters attracted to the attention of many researchers like^{48–52}.

Examination of these studies shows that incompressible 3-D tangent hyperbolic nanofluid flowing across a permeable surface with higher-order reactions are not studied. It is accounted for the combined effect of heating the Joule heating and viscous dissipation in a porous medium with the effects of the heat source (sink), slip velocity, and thermal radiation. The governing equations of the problem are solved by converting PDEs into ODEs by utilizing similarity transformations. OHAM was also used for related similar solutions. The findings were presented by figures and tables for the different parameters. Numerical computations are determined and presented for the drag force, local Nusselt, and Sherwood numbers.

Problem analysis

Consider the steady, incompressible non-Newtonian hyperbolic tangent nanofluid flow through a porous extending surface (see Fig. 1) with the assumptions:

- The flow model is 3-D with the z -direction perpendicular to the surface which is extended in the xy -plane.
- The velocity of mass influx is $w = w_0$, where $w_0 < 0$ mentioned for injection, and $w_0 > 0$ is for suction.
- Joule heating, MHD flow, higher-order chemical reaction, and viscous dissipation are considered in a porous medium.

The boundary-layer equations system of mass, motion, heat, and volume concentration for the flow under the above aspects according to Buongiorno model are^{37,41,49,51}:

$$\frac{\partial u}{\partial x} + \frac{\partial v}{\partial y} + \frac{\partial w}{\partial z} = 0, \tag{1}$$

$$u \frac{\partial u}{\partial x} + v \frac{\partial u}{\partial y} + w \frac{\partial u}{\partial z} = \nu(1-n) \frac{\partial^2 u}{\partial z^2} + n\nu\sqrt{2}\Gamma \frac{\partial u}{\partial z} \frac{\partial^2 u}{\partial z^2} - \frac{\sigma B_0^2}{\rho} u - \frac{\nu}{K_1} u, \tag{2}$$

$$u \frac{\partial v}{\partial x} + v \frac{\partial v}{\partial y} + w \frac{\partial v}{\partial z} = \nu(1-n) \frac{\partial^2 v}{\partial z^2} + n\nu\sqrt{2}\Gamma \frac{\partial v}{\partial z} \frac{\partial^2 v}{\partial z^2} - \frac{\sigma B_0^2}{\rho} v - \frac{\nu}{K_1} v \tag{3}$$

$$u \frac{\partial T}{\partial x} + v \frac{\partial T}{\partial y} + w \frac{\partial T}{\partial z} = \alpha \frac{\partial^2 T}{\partial z^2} + \tau \left[D_B \frac{\partial C}{\partial z} \frac{\partial T}{\partial z} + \frac{D_T}{T_\infty} \left(\frac{\partial T}{\partial z} \right)^2 \right] + \frac{\sigma B_0^2}{\rho c_p} u^2 + \frac{Q}{\rho c_p} (T - T_\infty) - \frac{1}{\rho c_p} \frac{\partial q_r}{\partial z} + \frac{\nu}{c_p} (1-n) \left(\frac{\partial u}{\partial z} \right)^2, \tag{4}$$

$$u \frac{\partial C}{\partial x} + v \frac{\partial C}{\partial y} + w \frac{\partial C}{\partial z} = D_B \frac{\partial^2 C}{\partial z^2} + \frac{D_T}{T_\infty} \frac{\partial^2 T}{\partial z^2} - k_c (C - C_\infty)^m. \tag{5}$$

The related boundary conditions are

$$\left. \begin{aligned} u &= u_w(x) = ax + N_1 \alpha \frac{\partial u}{\partial z}, v = v_w(y) = by + N_2 \alpha \frac{\partial v}{\partial z}, \\ w &= w_0, T = T_w, D_B \frac{\partial C}{\partial z} + \frac{D_T}{T_\infty} \frac{\partial T}{\partial z} = 0 \text{ at } z = 0, \\ u &\rightarrow 0, v \rightarrow 0, T \rightarrow T_\infty, C \rightarrow C_\infty \text{ as } z \rightarrow \infty, \end{aligned} \right\} \tag{6}$$

where u , v , and w are the velocity coordinates of along the orientations of x -, y -, and z -coordinates, respectively. Further, suppose that $u_w(x) = ax$ and $v_w(y) = by$, anywhere $a > 0$, and b is a constant, when ($b > 0$) agrees with an extending surface and whilst ($b < 0$) matches to a shrinking surface. The condition $D_B \frac{\partial C}{\partial z} + \frac{D_T}{T_\infty} \frac{\partial T}{\partial z} = 0$ at $z = 0$ physically implies that the nanoparticle fraction at the wall is measured passively. This condition provides for a random motion of nanoparticles at the boundary-layer. According to the Rosseland approximation, q_r is calculated as:

$$q_r = -\frac{4\sigma^*}{3k^*} \frac{\partial T^4}{\partial z}. \tag{7}$$

Supposing that temperature variance within the flux is such that T^4 can be prolonged in a Taylor-series about T_∞ and disregarding higher-order relationships. This outcome is the subsequent approximation: $T^4 \cong 4T_\infty^3 T - 3T_\infty^4$. Then, the relation (7) can be rewritten as $\frac{\partial q_r}{\partial z} = -\frac{16\sigma^* T_\infty^3}{3k^*} \frac{\partial^2 T}{\partial z^2}$ and moreover the heat relation (4) becomes in the formula:

$$u \frac{\partial T}{\partial x} + v \frac{\partial T}{\partial y} + w \frac{\partial T}{\partial z} = \left(\alpha + \frac{1}{\rho c_p} \frac{16\sigma^* T_\infty^3}{3k^*} \right) \frac{\partial^2 T}{\partial z^2} + \tau \left[D_B \frac{\partial C}{\partial z} \frac{\partial T}{\partial z} + \frac{D_T}{T_\infty} \left(\frac{\partial T}{\partial z} \right)^2 \right] + \frac{\sigma B_0^2}{\rho c_p} u^2 + \frac{Q}{\rho c_p} (T - T_\infty) + \frac{\nu}{c_p} (1-n) \left(\frac{\partial u}{\partial z} \right)^2. \tag{8}$$

Similarity transformations. Applying the next similarity transformations to the equations of the model and the associated boundary-conditions⁵¹,

$$\left. \begin{aligned} u &= axf'(\eta), v = ayg'(\eta), w = -\sqrt{a\alpha} [f(\eta) + g(\eta)], \eta = \sqrt{\frac{a}{\alpha}} z \\ \theta(\eta) &= \frac{T - T_\infty}{T_w - T_\infty}, \phi(\eta) = \frac{C - C_\infty}{C_w - C_\infty}, \end{aligned} \right\} \tag{9}$$

where the primes (') signify the differentiation with respect to η .

The flow model Eqs. (1-6) becomes:

$$[(1-n) + nWe_x f'''] Pr f'''' - f'^2 + (f+g)f'' - Mf' - Kf' = 0, \tag{10}$$

$$(f+g)g'' - g'^2 + [(1-n) + nWe_y g'''] Pr g'''' - Mg' - Kg' = 0, \tag{11}$$

$$\left(1 + \frac{4}{3}R_d\right)\theta'' + (f + g)\theta' + N_b\theta'\phi' + N_t\theta'^2 + MEcf'^2 + S\theta + (1 - n)PrEc f'^2 = 0, \tag{12}$$

$$\phi'' + Le(f + g)\phi' + \frac{N_t}{N_b}\theta'' - \gamma Le\phi^m = 0 \tag{13}$$

and the boundary-conditions in dimensionless forms are

$$\left. \begin{aligned} f'(0) &= 1 + \delta_1 f''(0), \quad g'(0) = \lambda + \delta_2 g''(0), \quad f(0) = f_w, \\ g(0) &= 0, \quad \theta(0) = 1, \quad \phi'(0) + \frac{N_t}{N_b}\theta'(0) = 0, \\ f'(\infty) &= 0, \quad g'(\infty) = 0, \quad \theta(\infty) = 0, \quad \phi(\infty) = 0, \end{aligned} \right\} \tag{14}$$

where λ characterizes the constant parameter of the sheet, where $\lambda > 0$ implies an extending plate whereas $\lambda < 0$ is exposes a shrinking plate. In this investigation, f_w represents the suction (injection) parameter, somewhere $f_w > 0$ resembles to suction, whilst $f_w < 0$ sympathizes to the blowing and $f_w = 0$ signifies an impermeable sheet. The values of used parameters are known as follows:

$$\begin{aligned} Pr &= \frac{\nu}{\alpha}, \quad We_x = \sqrt{2\frac{a}{\alpha}}a\Gamma x, \quad We_y = \sqrt{2\frac{a}{\alpha}}a\Gamma y, \quad M = \frac{\sigma B_0^2}{a\rho}, \quad K = \frac{\nu}{aK_1}, \quad \delta_1 = \sqrt{a\alpha}N_1, \quad \delta_2 = \sqrt{a\alpha}N_2, \quad \lambda = \frac{b}{a}, \\ f_w &= \frac{-w_0}{\sqrt{a\alpha}}, \quad Le = \frac{\alpha}{D_B}, \quad N_b = \frac{\tau D_B(C_w - C_\infty)}{\alpha}, \quad N_t = \frac{\tau D_T(T_w - T_\infty)}{\alpha T_\infty}, \quad R_d = \frac{4\sigma^* T_\infty^3}{3k^*k}, \quad Ec = \frac{u_w^2}{c_p(T_w - T_\infty)} \\ S &= \frac{Q}{a\rho c_p}, \quad \text{and } \gamma = \frac{k_c(C_w - C_\infty)^{m-1}}{a}. \end{aligned}$$

Drag force, heat and mass transfer. The drag force coefficients C_{fx} , C_{fy} , the Nusselt Nu_x and the Sherwood numbers Sh_x are specified as⁴⁹

$$C_{fx} = \frac{\tau_{wx}}{\rho U_w^2}, \quad C_{fy} = \frac{\tau_{wy}}{\rho V_w^2}, \quad Nu_x = \frac{xq_w}{k(T_w - T_\infty)} \quad \text{and} \quad Sh_x = \frac{xq_m}{D_B(C_w - C_\infty)}, \tag{15}$$

wherever τ_{wx} and τ_{wy} are the coefficients of skin friction in the x and y coordinates, q_w and q_m are the heat and mass fluxes from the wall of the surface. These are given as⁴⁹

$$\left. \begin{aligned} \tau_{wx} &= \mu \left[(1 - n) \frac{\partial u}{\partial z} + \frac{n\Gamma}{\sqrt{2}} \left(\frac{\partial u}{\partial z} \right)^2 \right]_{z=0}, \quad \tau_{wy} = \mu \left[(1 - n) \frac{\partial v}{\partial z} + \frac{n\Gamma}{\sqrt{2}} \left(\frac{\partial v}{\partial z} \right)^2 \right]_{z=0} \\ q_w &= -k \left(\frac{\partial T}{\partial z} \right)_{z=0}, \quad q_m = -D_B \left(\frac{\partial C}{\partial z} \right)_{z=0}, \end{aligned} \right\} \tag{16}$$

$$\left(\frac{Re_x}{Pr} \right)^{1/2} C_{fx} = \left[(1 - n)f''(0) + \frac{nWe_x}{2} f'^2(0) \right], \tag{17}$$

$$\left(\frac{Re_y}{Pr} \right)^{1/2} (\lambda)^{3/2} C_{fy} = \left[(1 - n)g''(0) + \frac{nWe_y}{2} g'^2(0) \right] \tag{18}$$

$$Nu_x = - \left(1 + \frac{4}{3}R_d \right) (Pr Re_x)^{1/2} \theta'(0), \tag{19}$$

$$Sh_x = -(Pr Re_x)^{1/2} \phi'(0), \tag{20}$$

where $Re_x = \frac{xu_w}{\nu}$ and $Re_x = \frac{y'v_w}{\nu}$ are the local Reynolds numbers.

Homotopic solution

Today, the computational methods used to solve the non-linear equations usually use approximations for non-linear terms or solutions to discretization or linearization. In engineering, challenges occur, and traditional numerical methods cannot always be used to address technology. Researchers have taken a tremendous interest in the analytical solution of these kinds of nonlinear issues over the last few decades. HAM is a type of method of analytical approximation majorly for non-linear differential equations. Observe that HAM utilizes a much more complicated equation of homotopy than for the continuation method of homotopy. In addition, the HAM gives greater freedom to choose the linear auxiliary operator. Most notably, the so-named convergence control parameter is introduced in the homotopy equation for the first time, such that the HAM affords us with an unpretentious way to ensure sequence convergence. The fundamental concept behind the method of analyzing homotopy is given by Liao⁵³. He applied a definition of topology renowned as homotopy. He exercised two distinct continuous functions specified by $\zeta_1(\tilde{x})$ and $\zeta_2(\tilde{x})$ via the two spaces \tilde{X} and \tilde{Y} . The general structure of the transformation is depending on connecting the closed unit interval with the defined topological spaces, as shown below:

$$\tilde{\Psi} : \hat{X} \times [0, 1] \rightarrow \hat{Y} \tag{21}$$

where $\tilde{\Psi}[\tilde{x}, 0] = \zeta_1(\tilde{x})$ and $\tilde{\Psi}[\tilde{x}, 1] = \zeta_2(\tilde{x}), \forall \tilde{x} \in \hat{X}$. In Eq. (20), the given process is called a homotopic conversion. The system of ODEs (10)–(13) with the boundary conditions (14) are resolved by OHAM, with selecting appropriate initial estimations f_0, g_0, θ_0 and ϕ_0 with the consistent linear operators specified as:

$$f_0 = 1 - e^{-\eta}, g_0 = \lambda(1 - e^{-\eta}), \theta_0 = e^{-\eta}, \text{ and } \phi_0 = \frac{N_t}{N_b} e^{-\eta} \tag{22}$$

$$L_f = (D^3 - D)f, L_g = (D^3 - D)g, L_\theta = (D^2 - D)\theta, \text{ and } L_\phi = (D^2 - D)\phi \tag{23}$$

with

$$\left. \begin{aligned} L_f &= \left(\sum_{i=0}^2 \mathfrak{D}_{i+1} e^{(i-1)\eta} \right) = 0, \\ L_g &= \left(\sum_{i=0}^2 \mathfrak{D}_{i+4} e^{(i-1)\eta} \right) = 0, \\ L_\theta &= \left(\sum_{i=2}^3 \mathfrak{D}_{i+5} e^{(-1)^i \eta} \right) = 0, \\ L_\phi &= \left(\sum_{i=2}^3 \mathfrak{D}_{i+7} e^{(-1)^i \eta} \right) = 0, \end{aligned} \right\} \tag{24}$$

where \mathfrak{D}_i ($i = 1 - 10$) signify the constants
The errors are appointed in N th-order as:

$$e_N^f = \frac{1}{k+1} \sum_{i=0}^k \left[N_f \left(\sum_{j=0}^N (\hat{f}_j)_{\eta=i\pi\eta}, \sum_{j=0}^N (\hat{g}_j)_{\eta=i\pi\eta} \right) \right]^2 \tag{25}$$

$$e_N^g = \frac{1}{k+1} \sum_{i=0}^k \left[N_g \left(\sum_{j=0}^N (\hat{f}_j)_{\eta=i\pi\eta}, \sum_{j=0}^N (\hat{g}_j)_{\eta=i\pi\eta} \right) \right]^2 \tag{26}$$

$$e_N^\theta = \frac{1}{k+1} \sum_{i=0}^k \left[N_\theta \left(\sum_{j=0}^N (\hat{f}_j)_{\eta=i\pi\eta}, \sum_{j=0}^N (\hat{g}_j)_{\eta=i\pi\eta}, \sum_{j=0}^N (\hat{\theta}_j)_{\eta=i\pi\eta}, \sum_{j=0}^N (\hat{\phi}_j)_{\eta=i\pi\eta} \right) \right]^2 \tag{27}$$

$$e_N^\phi = \frac{1}{k+1} \sum_{i=0}^k \left[N_\phi \left(\sum_{j=0}^N (\hat{f}_j)_{\eta=i\pi\eta}, \sum_{j=0}^N (\hat{g}_j)_{\eta=i\pi\eta}, \sum_{j=0}^N (\hat{\theta}_j)_{\eta=i\pi\eta}, \sum_{j=0}^N (\hat{\phi}_j)_{\eta=i\pi\eta} \right) \right]^2 \tag{28}$$

$$e_N^t = e_N^f + e_N^g + e_N^\theta + e_N^\phi \tag{29}$$

where e_N^t describes the sum of square remaining error. The main purpose is to accomplish optimum converged parameters by reducing the average square residues in total. The variable \hbar is called the convergence control plays a crucial part. At 4th-order of computations, the squared residual errors $\hbar_f, \hbar_g, \hbar_\theta, \hbar_\phi$ are $\hbar_f = -1.499782, \hbar_g = -1.070914, \hbar_\theta = -0.849217$ and $\hbar_\phi = -0.938912$ and the average sum of square residual error is $e_N^t = 1.70109 \times 10^{-5}$. Figure 2 achieves the sum average of residual errors when $Pr = 6.2, M = \delta_1 = 1.0, f_w = 2.5, S = -0.5, \delta_2 = -2.5, \lambda = -0.1, n = 0.1, Ec = 0.5, We_x = We_y = 0.3, K = R_d = N_t = N_b = 0.5, m = 2.0, \gamma = 1.0,$ and $Le = 5$. Table 1 demonstrates residual errors with similar parametric quantities as stated above for different approximation orders.

Results and discussion

This section demonstrates and discusses the outcomes of several leading parameters on the field of flow. We have organized our results by putting $Pr = 6.2, M = 1.0, \delta_1 = 1.0, R_d = 0.5, K = 0.5, f_w = 2.5, S = -0.5, \delta_2 = -2.5, \lambda = -0.1, n = 0.1, Ec = 0.5, We_x = We_y = 0.3, N_t = N_b = 0.5, m = 2.0, \gamma = 1.0,$ and $Le = 5$ except if specified otherwise. A comparison is exhibited in Table 2 in order to access the verification of the code of our study. The values of drag force for diverse values of M taking the related parameters as $Pr = 1, n = 0, f_w = 0, \delta_1 = 0, \delta_2 = 0, \lambda = 0, K = 0, Ec = 0, S = 0, \gamma = 0, R_d = 0$ and $We_x = We_y = 0$. These values have been compared and showed excellent accord with Ref.⁴⁸ and Ref.⁵¹.

Impact of porous material parameter K . Figure 3 reveals the velocities profile for different values of a porous material parameter K . It is found that the x and y -axes velocities reduce with K , and $f'(\eta)$ existence on the upper side. Thus, the thickness of the momentum's boundary-layer is reduced, and less volume from the nanofluid is fluxed. The cause behind the physical phenomenon is the pores of a porous material that declines the velocities. The effects are clear and distinct close to the surface. Pictographic proofs also reveal that nanofluid

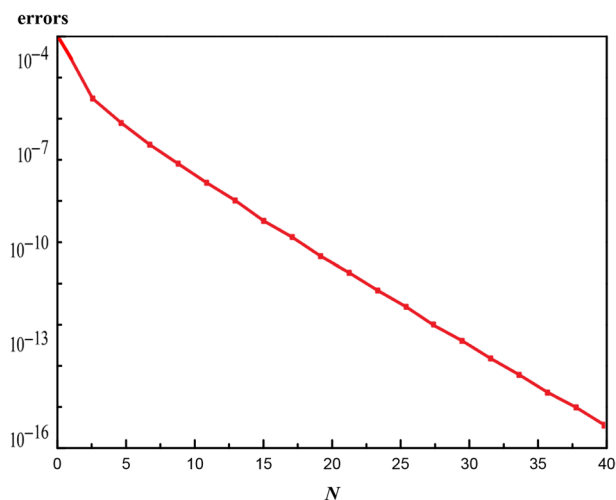


Figure 2. Sum average of residual squared errors.

N	e_N^f	e_N^g	e_N^θ	e_N^ϕ
4	7.37908×10^{-7}	5.15601×10^{-7}	6.56997×10^{-6}	9.12325×10^{-6}
10	5.14596×10^{-10}	4.11797×10^{-10}	3.55419×10^{-8}	9.2597×10^{-8}
20	7.93954×10^{-13}	2.38014×10^{-14}	2.97324×10^{-11}	8.930159×10^{-11}
30	1.40898×10^{-15}	8.6531×10^{-17}	5.06211×10^{-14}	1.50661×10^{-13}
40	3.18976×10^{-18}	4.58403×10^{-20}	9.82761×10^{-17}	2.77921×10^{-16}

Table 1. Averaged residual squared errors taking into account the desired auxiliary number values.

M	Ref. ⁴⁸	Ref. ⁵¹	Present outcomes
0	-1.00000	-1.00001	-1.0000097
0.25	-1.11803	-1.11803	-1.1180333
1	-1.41421	-1.41421	-1.4142105
5	-2.44949	-2.44949	-2.4494932
10	-3.31662	-3.31663	-3.3166265
50	-7.14142	-7.14143	-7.1414259
100	-10.0499	-10.0499	-10.049894
500	-22.383	-22.383	-22.383134
1,000	-31.6386	-31.6386	-31.638602

Table 2. Comparison of drag force coefficient for distinct values of M when Pr = 1, n = 0, f_w = 0, δ₁ = 0, δ₂ = 0, λ = 0, K = 0, Ec = 0, S = 0, γ = 0, R_d = 0 and We_x = We_y = 0.

has a high velocity in x-direction $f'(\eta)$ relative to the y-velocity $g'(\eta)$. The profile of temperature $\theta(\eta)$ as we displayed in Fig. 4 depicts that the temperature of the nanofluid raises because of the escalating behavior of K. Within $1.0 \leq \eta \leq 4.0$ (not precisely specified), the influence is very obvious and significant. The curve converges smoothly to zero outside the area described above, namely $\eta > 4.0$. Figure 5 elaborates the concentration distribution $\phi(\eta)$ for growing the value of K. In the interior range $0.0 \leq \eta \leq 1.5$ (not precisely specified) the influence is distinguished but for $\eta > 1.5$, the curve is stable and asymptotically inclining to zero. This figure manifests that the nanofluid concentration is diminished more rapidly than that for the case without porous material. The reduced number of Sherwood Sh_x should be noted is reduced for the mounting style of K.

Impact of suction (blowing) f_w . Figure 6 offers the velocities profile for distinct values of a suction (blowing) parameter f_w . It is remarked that the x and y-directions flow velocities diminish with f_w , and $f'(\eta)$ existence on the top part. Thus, the thickness of the corresponding boundary-layer is reduced too, and the blowing ($f_w < 0$) is a higher velocity than the suction ($f_w > 0$). The cause behind the physical phenomenon is the pores of a porous material that declines the velocities. The influences are strong and distinct close to the surface especially in $g'(\eta)$. The profile of temperature $\theta(\eta)$ as exhibited in Fig. 7 addresses the temperature of the nanofluid

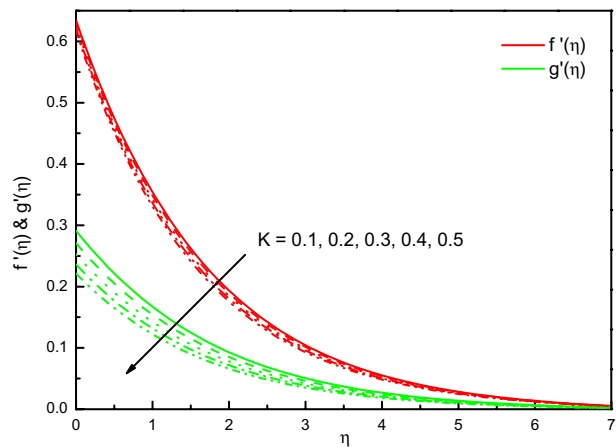


Figure 3. Graph of $f'(\eta)$ and $g'(\eta)$ vs. K .

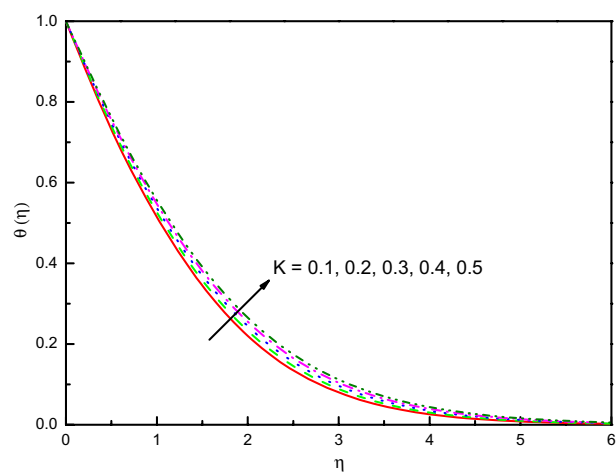


Figure 4. Graph of $\theta(\eta)$ vs. K .

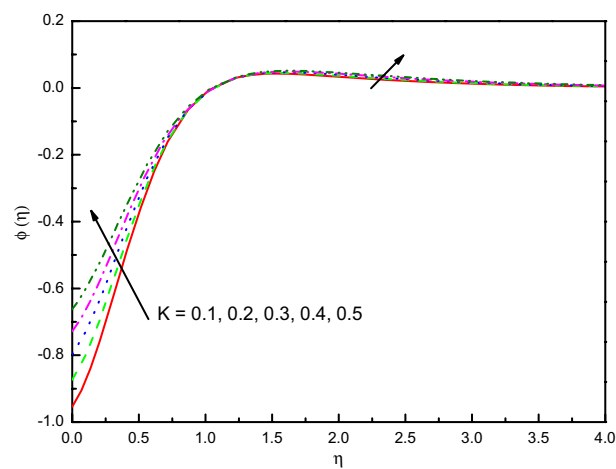


Figure 5. Graph of $\phi(\eta)$ vs. K .

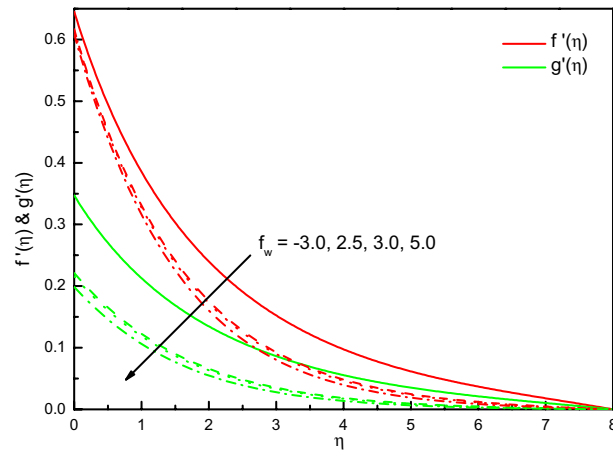


Figure 6. Graph of $f'(\eta)$ and $g'(\eta)$ vs. f_w .

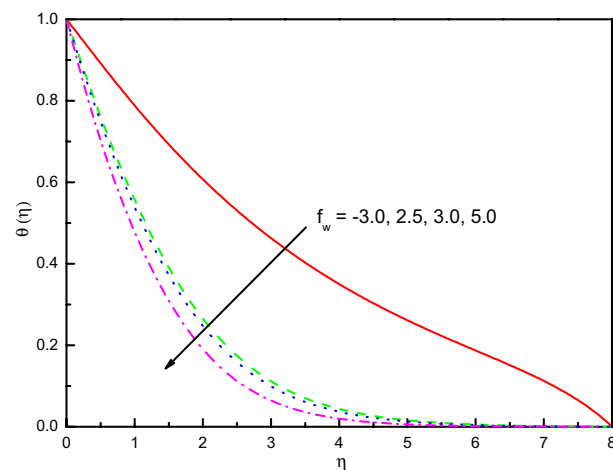


Figure 7. Graph of $\theta(\eta)$ vs. f_w .

diminishes cause of the intensifying behavior of f_w . Within $1.0 \leq \eta \leq 5.0$ (not precisely specified), the impact is very noticeable and significant. The curve converges smoothly to zero outside the area described above, namely $\eta > 5$. It obvious that the blowing effect (at $f_w = -0.3$) is not asymptote in the established boundary conditions of the problem, because doesn't meet the tolerance of computations and there may be no flow at this value experimentally. Figure 8 explains the reduction of concentration gradients $\phi(\eta)$ for rising the value of f_w . Inside the range $0.0 \leq \eta \leq 4.0$ (not precisely specified) the influence is illustrious but for $\eta > 4.0$, the curve is stable and asymptotically predisposing to zero. This figure establishes that the nanofluid concentration is raised than that of without suction (blowing). The rate of mass transfer that should be observed is raised for the escalating modality of f_w .

Impact of power-law index n . Figure 9 illustrates the influence of n on $f'(\eta)$ and $g'(\eta)$. Likewise, the non-Newtonian factor n amplification implicates high viscous properties in the nanofluid, and therefore reduces the impact. The results are transparent and distinct near to the wall. In graphical evidence, Newtonian nanofluid also acquires a high velocity compared to non-Newtonian nanofluid. This reduces the drag force's effectiveness on the surface by the Newtonian characteristic of the fluid. The temperature establishes to overabundant in Fig. 10 with the values of increment in n . In fact, the numerical findings support the important effects of nanofluid thermal properties on the consistency index n . Figure 11 indicates the concentration improved outlines and the consistent boundary-layer thickness. The rate of mass transfer is diminished with n rising values.

Impact of slip velocity δ_1 . Figure 12 elucidates that $f'(\eta)$ is declined with the upsurge of δ_1 parameter whilst, $g'(\eta)$ is raised with δ_1 . As δ_1 parameter is specified as $\sqrt{a\alpha}N_1$, an upsurge in the parameter δ_1 will affect in a rise in thermal diffusion α and hence the thermal conductivity. We can see that thermal diffusion is nothing but the measurement of resistance to nanofluid movement especially in the x -velocity but the effect on $g'(\eta)$ not clear relative to $f'(\eta)$. Therefore, δ_1 positive effect will certainly slow the nanofluid dominant velocity. The impact near

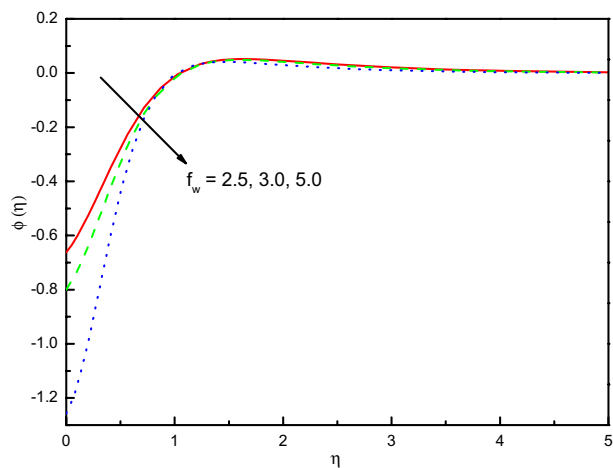


Figure 8. Graph of $\phi(\eta)$ vs. f_w .

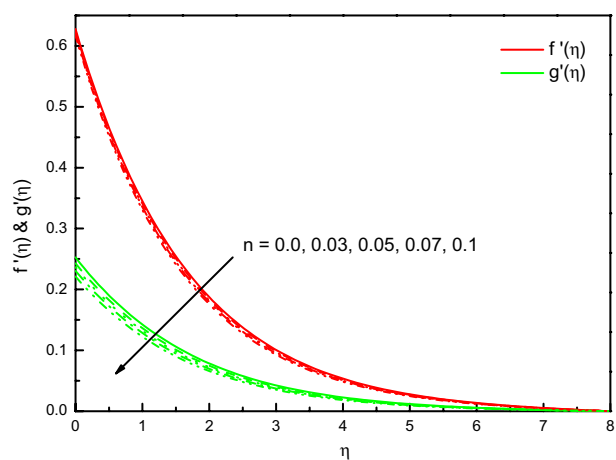


Figure 9. Graph of $f'(\eta)$ and $g'(\eta)$ vs. n .

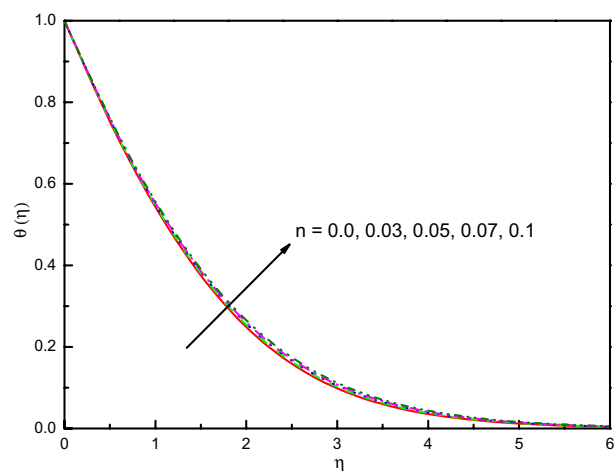


Figure 10. Graph of $\theta(\eta)$ vs. n .

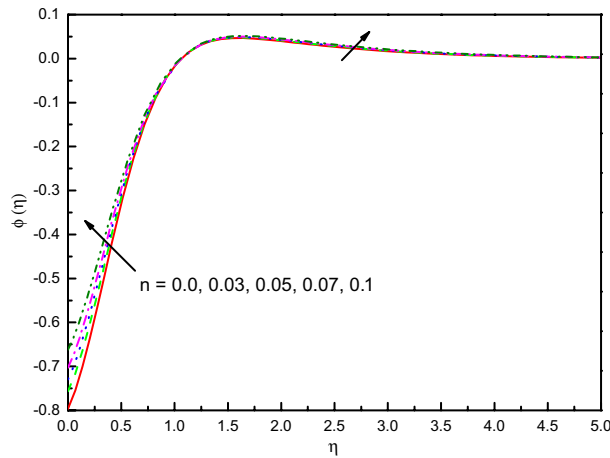


Figure 11. Graph of $\phi(\eta)$ vs. n .

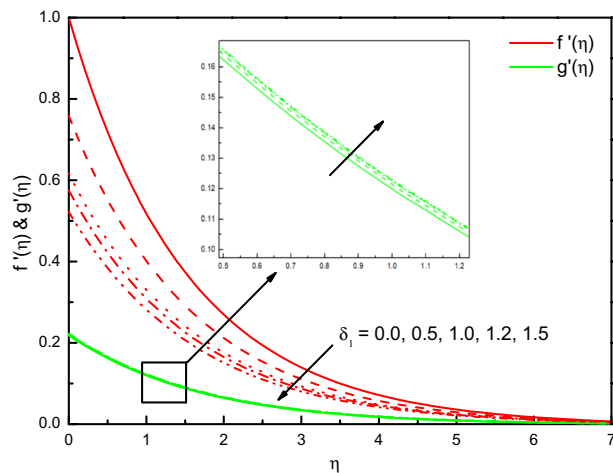


Figure 12. Graph of $f'(\eta)$ and $g'(\eta)$ vs. δ_1 .

to the surface is dominant, however further from the surface, it is diminished. Interestingly, the velocity of the Newtonian nanofluid in the boundary-layer region is altitude compared with others. Due to the resistivity force non-Newtonian nanofluid will be stronger because of the greater viscosity of it. The result is a higher velocity of the Newtonian nanofluids.

Figure 13 reveals that the profile of temperature is diminished into the boundary layer result in the positive impact of δ_1 , and by the condition $\eta \rightarrow \infty$, the temperature concurs fluently. Physically, it can be clarified that the temperature is decreased because the parameter δ_1 looks to be a desirable consideration for increasing thermal diffusion. It is decided that the rate of heat transport can be increased by δ_1 . The concentration outline $\phi(\eta)$ is magnified with the increment values of δ_1 as shown in Fig. 14. In the area $0.0 \leq \eta \leq 2.0$ (not precisely specified) the influence is eminent but in the area after $\eta = 2.0$, the curve is approximately stable and tends to zero. It is obvious from this figure that $\phi(\eta)$ of a nanofluid without slip velocity is less in comparison with δ_1 existence. Also, this gives us the expectation that Sh_x shrinkages due to the mounting behavior of δ_1 .

Impact of thermal radiation R_d , heat source S , and Eckert number Ec . Figure 15 discloses that the temperature for the nanofluid is raised due to the influence of thermal radiation parameter R_d . The impact within the region $1.0 \leq \eta \leq 4.0$ (approximately) is very significant and clear yet the curvature after that converges asymptotically to zero. This upsurges the thickening of the thermal boundary layer. The parameter R_d , i.e.

$R_d = \frac{4\sigma^* T_\infty^3}{3k^*k}$ allows us to obtain the physical evidence that the nanofluid thermal conductivity weakens immediately R_d rises because the frictional heat is decreased in the flow scheme. It is remarkable to remember that being extremely viscous in kind, hyperbolic tangent nanofluids produce more heat than Newtonian nanofluids. Figure 16 discloses that the concentration $\phi(\eta)$ diminishes in response to the non-negative values of R_d when $R_d > 0$. The nanofluid has a less concentration profile with R_d compared in the situation without R_d , this can be traced to a promisingly effective concentration within the area $0.0 \leq \eta \leq 2.5$ (not precisely specified).

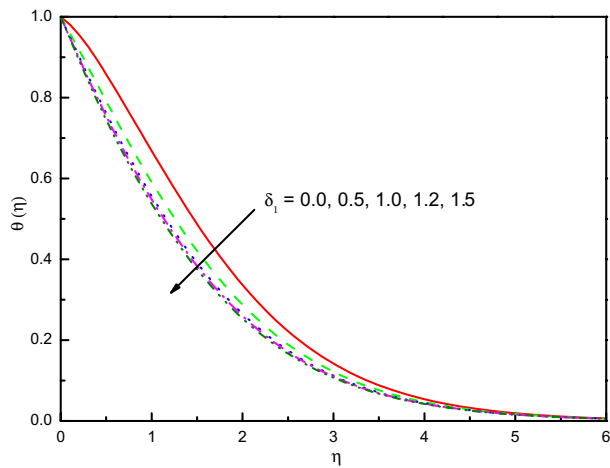


Figure 13. Graph of $\theta(\eta)$ vs. δ_1 .

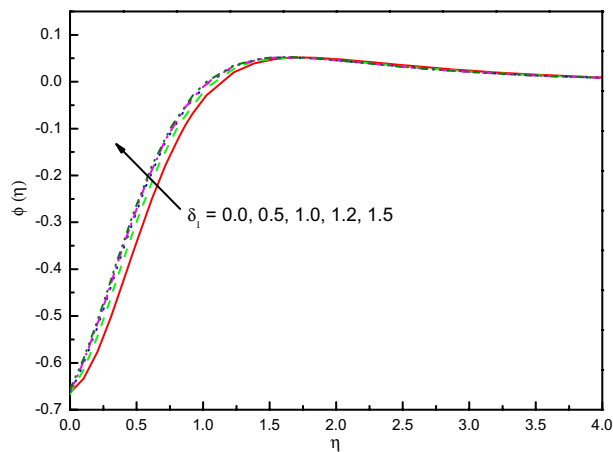


Figure 14. Graph of $\phi(\eta)$ vs. δ_1 .

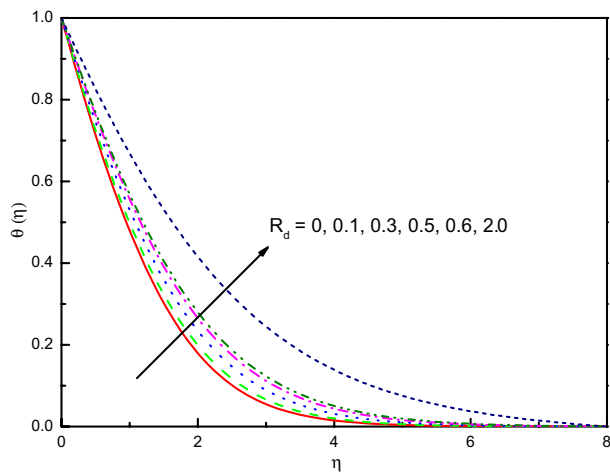


Figure 15. Graph of $\theta(\eta)$ vs. R_d .

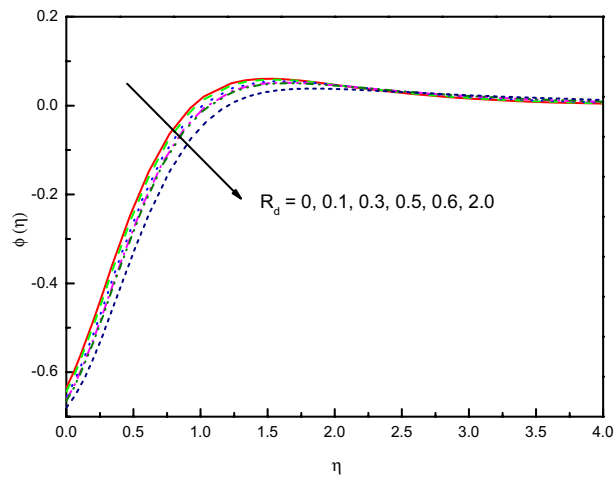


Figure 16. Graph of $\phi(\eta)$ vs. R_d .

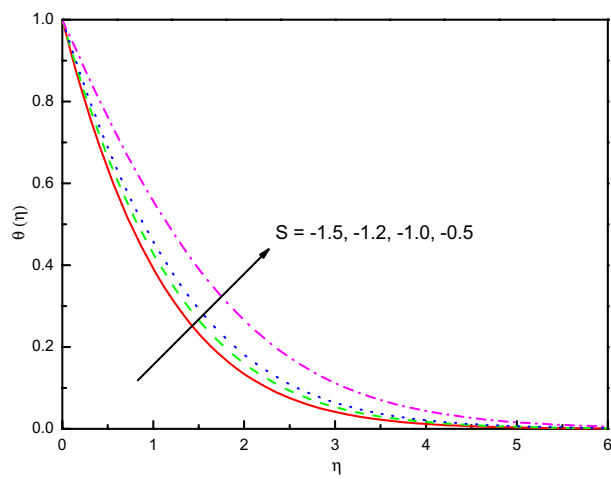


Figure 17. Graph of $\theta(\eta)$ vs. S .

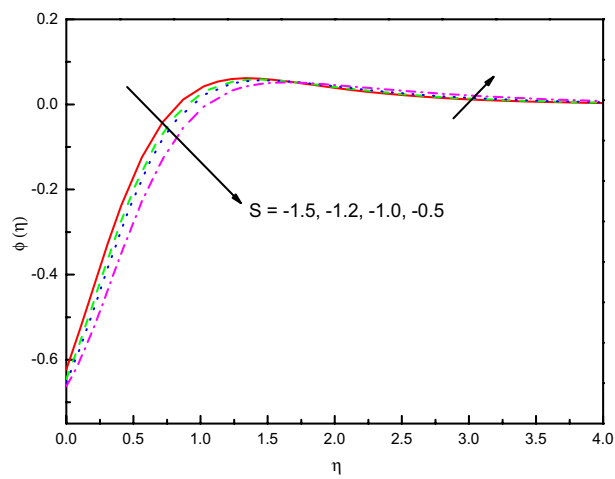


Figure 18. Graph of $\phi(\eta)$ vs. S .

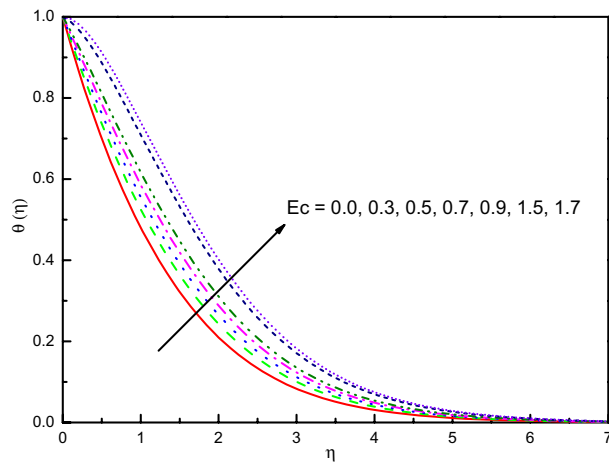


Figure 19. Graph of $\theta(\eta)$ vs. Ec .

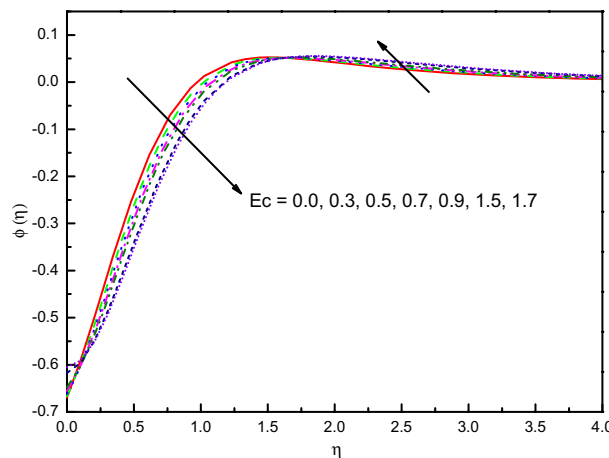


Figure 20. Graph of $\phi(\eta)$ vs. Ec .

The outcome of S on temperature and concentration outlines has been disclosed in Figs. 17 and 18, respectively. It is noticed that temperature tends to rise and concentration inclines to diminish and the influence is protuberant within section $0.0 \leq \eta \leq 2.5$. The curve then attains the boundary condition numerically and graphically. Correspondingly, the temperature and concentration distribution predominate much as we discussed in the absorption case. The same impact can be remarked in the case of growing values of Ec on the $\theta(\eta)$ and $\phi(\eta)$ which is displayed Figs. 19 and 20. But the higher Ec values are more clearly temperature than concentration, it is notable that after the value $\eta > 1.5$, the effect of the concentration is reversed. From Table 3, we see that $|\theta'(0)|$ declines for both R_d , S , and Ec .

Impact of chemical reaction γ and its order m . Figure 21 shows that in feedback to the positive method of parameter γ in $\gamma > 0$ (destructive reactions), the temperature in the 1st-order of reaction (i.e., $m = 1.0$) increases. In the area of $0.5 \leq \eta \leq 4.0$ (not precisely specified), the temperature is efficient auspiciously. Figure 22 reveals that the concentration is raised with the γ is the destructive case in the area $0.0 \leq \eta \leq 1.0$ approximately, after that the impact is reversed. Furthermore, the well-known formula between the parameter of the rate of chemical reaction and volume concentration is specified as $\gamma \propto (\phi)^m$, where m is the reaction order. The relationship offers that if γ increases, the concentration goes high in $\eta > 1.0$, after that is reversed until $\eta = 4$, then it converges to zero. But when we look at the destructive reaction ($\gamma > 0$), the result is totally reverse and some disturbance in the flow happened.

It is seen from Fig. 23 that the concentration of destructive ($\gamma = 1.0$) case upsurges in the most area of η but it is mentionable the impact m varies between the odd and even order when the order of the reaction increased. The impact is significantly eminent here on concentration. However, Fig. 24 for $\gamma = -1.0$ shows the opposite result. For $\gamma < 0.0$, In the area $0.0 \leq \eta \leq 2.5$ (approximately) the curve purely rises, but then the curve gradually reduces and converges to zero asymptotically. The concentration distribution is not so eminent in the situation

Ec	S	R_d				
		0.3	0.5	1.0	1.5	2.0
0.0	-0.5	0.5832	0.0253	0.4548	0.4027	0.3658
	-0.3	0.4491	0.0253	0.3523	0.3136	0.2865
	0.0	0.1109	0.1131	0.0253	0.1183	0.1195
	0.5	0.0330	0.1991	0.8399	5.4013	2.0063
0.1	-0.5	0.5786	0.5318	0.4520	0.4005	0.3640
	-0.3	0.4444	0.4092	0.3494	0.3113	0.2847
	0.0	0.1059	0.1088	0.1134	0.1159	0.1175
	0.5	0.0381	0.1951	0.8375	1.1382	2.1485
0.5	-0.5	0.5603	0.5163	0.4407	0.3916	0.3566
	-0.3	0.4256	0.3933	0.3379	0.3023	0.2772
	0.0	0.0856	0.0918	0.1012	0.1065	0.1098
	0.5	0.0585	0.1788	0.8280	1.1629	4.2189

Table 3. Variations of $|\theta'(0)|$ with Ec , S and R_d when $Pr = M = \gamma = m = K = 1$, $f_w = 2.5$, $\delta_1 = 1$, $\delta_2 = -2.5$, $\lambda = 0.1$, $n = 0.5$, $We_x = We_y = 0.3$, $N_f = N_b = 0.1$, and $Le = 5$.

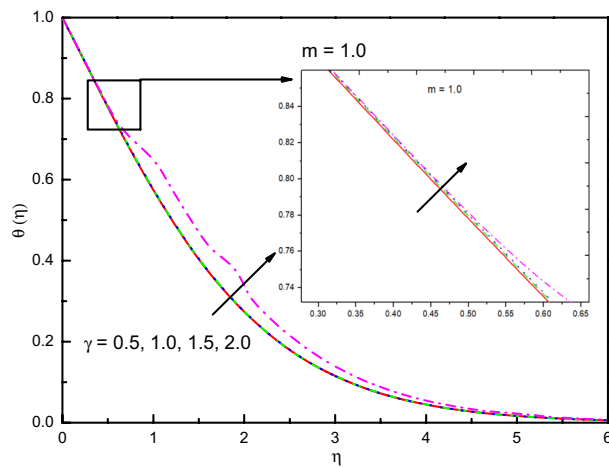


Figure 21. Graph of $\theta(\eta)$ vs. γ .

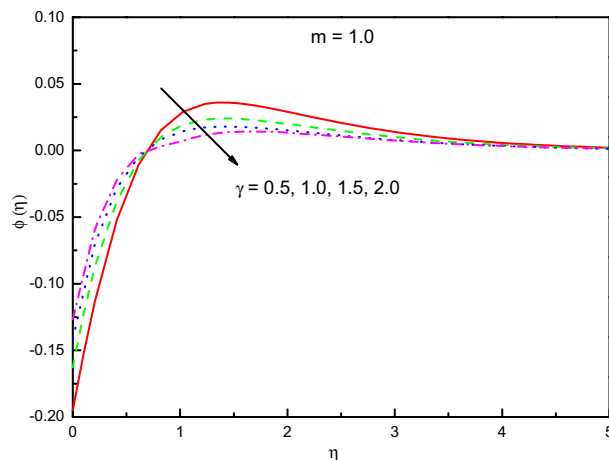


Figure 22. Graph of $\phi(\eta)$ vs. γ .

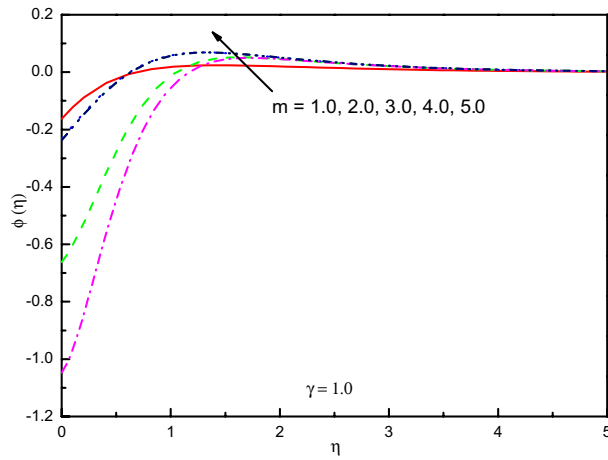


Figure 23. Graph of $\phi(\eta)$ vs. m (destructive reaction).

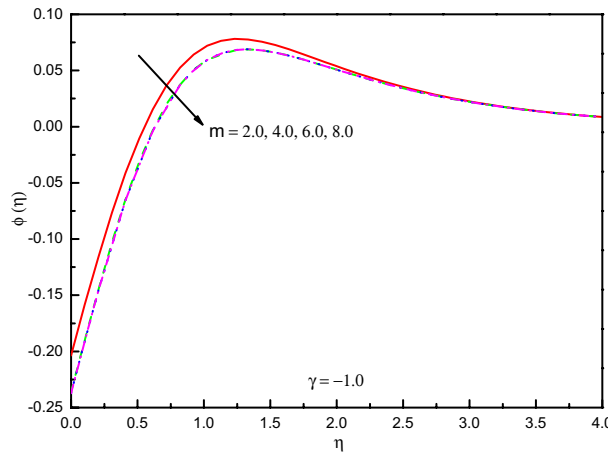


Figure 24. Graph of $\phi(\eta)$ vs. m (generative reaction).

Ec	m	γ				
		0.1	0.5	1.0	1.5	2.0
0.0	1.0	0.4468	0.4395	0.4366	0.4350	0.4339
	3.0	0.4486	0.4463	0.4453	0.4448	0.4443
	5.0	0.4481	0.4465	0.4459	0.4456	0.4453
	7.0	0.4475	0.4464	0.4459	0.4456	0.4455
0.5	1.0	0.4183	0.4111	0.4082	0.4067	0.4057
	3.0	0.4201	0.4178	0.4169	0.4163	0.4159
	5.0	0.4196	0.4181	0.4175	0.4171	0.4169
	7.0	0.4191	0.4179	0.4175	0.4172	0.4170
1.0	1.0	0.3898	0.3827	0.3798	0.3783	0.3774
	3.0	0.3916	0.3893	0.3884	0.3879	0.3874
	5.0	0.3911	0.3896	0.3890	0.3887	0.3884
	7.0	0.3906	0.3895	0.3890	0.3888	0.3886

Table 4. Variations of $|\phi'(0)|$ with Ec , m and γ when $Pr = M = \delta_1 = R_d = K = 1$, $f_w = 2.5$, $S = -0.5$, $\delta_2 = -2.5$, $\lambda = 0.1$, $n = 0.1$, $We_x = We_y = 0.3$, $N_t = N_b = 0.5$, and $Le = 5$.

of a generative reaction with m after $m > 4$. Table 4 confirms the graphical outcomes, whilst the rate of mass transport is diminished with γ in the case of a destructive reaction, this impact raises the rate with m and it varies with $m > 4$. In this case, it is obvious that Ec diminished the rate of mass transport.

Conclusions

Due to its extensive applications in cancer medications, drug delivery, polymers, and optical fiber, the new features of thermal ray and higher-order reactions in the flow behavior of non-Newtonian nanofluids are very interesting. The influence of thermal ray, and m th-order chemical reaction on hyperbolic tangent nanofluid flow in a porous material with heat generation (absorption), and Joule heating has been discussed by utilizing the OHAM. Some significant findings are listed on the basis of the entire investigation:

- The velocities distributions decline, when the parameter of porous material is escalated. The same behavior with δ_1 , f_w , and n , except the impact of δ_1 on the $g'(\eta)$.
- Temperature improves with increasing values of K , n , and the generative reaction case. But the reverse state occurs with f_w , δ_1 , and the destructive reaction.
- Concentration diminishes with R_d , Ec , and the destructive reaction, but the reversed effect observes with n and m (destructive state). The increment is significant with K and δ_1 , whereas f_w and S offer reducing phenomenon near the boundary-layer.
- Nusselt number reduces in the existence of R_d , Ec and S parameters, whilst the contrary state happens in the situation of f_w .
- Sherwood number reinforces with Ec , and R_d are increased. Nonetheless, the opposite influence is featured with K and m in the case of destructive reaction.

Received: 18 June 2020; Accepted: 18 August 2020

Published online: 03 September 2020

References

- Schlichting, H. *Boundary Layer Theory* Vol. 7 (McGraw-Hill, New York, 1960).
- Sakiadis, B. C. Boundary-layer behavior on continuous solid surfaces: I. Boundary-layer equations for two-dimensional and axisymmetric flow. *AIChE J.* **7**, 26–28 (1961).
- Sakiadis, B. C. Boundary-layer behavior on continuous solid surfaces: II. The boundary layer on a continuous flat surface. *AIChE J.* **7**, 221–225 (1961).
- Crane, L. J. Flow past a stretching plate. *Z. Angew. Math. Phys. ZAMP* **21**, 645–647 (1970).
- Gupta, P. & Gupta, A. Heat and mass transfer on a stretching sheet with suction or blowing. *Can. J. Chem. Eng.* **55**, 744–746 (1977).
- Dutta, B., Roy, P. & Gupta, A. Temperature field in flow over a stretching sheet with uniform heat flux. *Int. Commun. Heat Mass Transf.* **12**, 89–94 (1985).
- Cortell, R. Effects of viscous dissipation and work done by deformation on the MHD flow and heat transfer of a viscoelastic fluid over a stretching sheet. *Phys. Lett. A* **357**, 298–305 (2006).
- Ibrahim, F., Hady, F., Abdel-Gaied, S. & Eid, M. R. Influence of chemical reaction on heat and mass transfer of non-Newtonian fluid with yield stress by free convection from vertical surface in porous medium considering Soret effect. *Appl. Math. Mech.* **31**, 675–684 (2010).
- Hady, F., Ibrahim, F., Abdel-Gaied, S. & Eid, M. R. Influence of yield stress on free convective boundary-layer flow of a non-Newtonian nanofluid past a vertical plate in a porous medium. *J. Mech. Sci. Technol.* **25**, 2043 (2011).
- Hady, F., Ibrahim, F., Abdel-Gaied, S. & Eid, M. R. Boundary-layer non-Newtonian flow over vertical plate in porous medium saturated with nanofluid. *Appl. Math. Mech.* **32**, 1577–1586 (2011).
- Gholinia, M., Kiaeian Moosavi, S., Gholinia, S. & Ganji, D. Numerical investigation of heat transfers in the water jacket of heavy duty diesel engine by considering boiling phenomenon. *Case Stud. Therm. Eng.* **12**, 497–509 (2018).
- Gholinia, M., Kiaeian Moosavi, S., Gholinia, S. & Ganji, D. Numerical simulation of nanoparticle shape and thermal ray on a CuO/C₂H₆O₂-H₂O hybrid base nanofluid inside a porous enclosure using Darcy's law. *Heat Transf. Asian Res.* **48**, 3278–3294 (2019).
- Gholinia, M., Kiaeian Moosavi, S., Pourfallah, M., Gholinia, S. & Ganji, D. A numerical treatment of the TiO₂/C₂H₆O₂-H₂O hybrid base nanofluid inside a porous cavity under the impact of shape factor in MHD flow. *Int. J. Ambient Energy* <https://doi.org/10.1080/01430750.2019.1614996> (2019).
- Gholinia, M., Armin, M., Ranjbar, A. & Ganji, D. Numerical thermal study on CNTs/C₂H₆O₂-H₂O hybrid base nanofluid upon a porous stretching cylinder under impact of magnetic source. *Case Stud. Therm. Eng.* **14**, 100490 (2019).
- Gholinia, M., Hosseinzadeh, K. & Ganji, D. Investigation of different base fluids suspend by CNTs hybrid nanoparticle over a vertical circular cylinder with sinusoidal radius. *Case Stud. Therm. Eng.* **21**, 100666 (2020).
- Ghadikolaie, S. & Gholinia, M. 3D mixed convection MHD flow of GO-MoS₂ hybrid nanoparticles in H₂O-(CH₂OH)₂ hybrid base fluid under the effect of H₂ bond. *Int. Commun. Heat Mass Transf.* **110**, 104371 (2020).
- Hady, F., Ibrahim, F., Abdel-Gaied, S. & Eid, M. R. Boundary-layer flow in a porous medium of a nanofluid past a vertical cone. In *An Overview of Heat Transfer Phenomena* (ed. Kazi, S. N.) 91–104 (Intech Open, London, 2012).
- Hady, F., Ibrahim, F., Abdel-Gaied, S. & Eid, M. R. Effect of heat generation/absorption on natural convective boundary-layer flow from a vertical cone embedded in a porous medium filled with a non-Newtonian nanofluid. *Int. Commun. Heat Mass Transf.* **38**, 1414–1420 (2011).
- Aftab, W. *et al.* Nanoconfined phase change materials for thermal energy applications. *Energy Environ. Sci.* **11**, 1392–1424 (2018).
- Hady, F., Ibrahim, F., Abdel-Gaied, S. & Eid, M. R. Radiation effect on viscous flow of a nanofluid and heat transfer over a nonlinearly stretching sheet. *Nanoscale Res. Lett.* **7**(1), 229 (2012).
- Kumar, S. G. *et al.* Three-dimensional conducting flow of radiative and chemically reactive Jeffrey fluid through porous medium over a stretching sheet with Soret and heat source/sink effects. *Results Eng.* <https://doi.org/10.1016/j.rineng.2020.100139> (2020).
- Hamid, M., Usman, M., Khan, Z., Haq, R. & Wang, W. Heat transfer and flow analysis of Casson fluid enclosed in a partially heated trapezoidal cavity. *Int. Commun. Heat Mass Transf.* **108**, 104284 (2019).
- Hamid, M., Usman, M., Haq, R., Khan, Z. & Wang, W. Wavelet analysis of stagnation point flow of non-Newtonian nanofluid. *Appl. Math. Mech.* **40**, 1211–1226 (2019).
- Khan, Z. H., Khan, W. A. & Hamid, M. Non-Newtonian fluid flow around a Y-shaped fin embedded in a square cavity. *J. Therm. Anal. Calorim.* <https://doi.org/10.1007/s10973-019-09201-9> (2020).

25. Eid, M. R. & Makinde, O. Solar radiation effect on a magneto nanofluid flow in a porous medium with chemically reactive species. *Int. J. Chem. Reactor Eng.* **16**, 20170212 (2018).
26. Eid, M. R., Al-Hossainy, A. & Zoromba, M. S. FEM for blood-based SWCNTs flow through a circular cylinder in a porous medium with electromagnetic radiation. *Commun. Theor. Phys.* **71**, 1425 (2019).
27. Eid, M. R. Chemical reaction effect on MHD boundary-layer flow of two-phase nanofluid model over an exponentially stretching sheet with a heat generation. *J. Mol. Liq.* **220**, 718–725 (2016).
28. Eid, M. R. & Mahny, K. L. Unsteady MHD heat and mass transfer of a non-Newtonian nanofluid flow of a two-phase model over a permeable stretching wall with heat generation/absorption. *Adv. Powder Technol.* **28**, 3063–3073 (2017).
29. Durgaprasad, P., Varma, S., Hoque, M. M. & Raju, C. Combined effects of Brownian motion and thermophoresis parameters on three-dimensional (3D) Casson nanofluid flow across the porous layers slendering sheet in a suspension of graphene nanoparticles. *Neural Comput. Appl.* **31**, 6275–6286 (2019).
30. Prasad, P. D., Kumar, R. K. & Varma, S. Heat and mass transfer analysis for the MHD flow of nanofluid with radiation absorption. *Ain Shams Eng. J.* **9**, 801–813 (2018).
31. Wakif, A., Boulahia, Z., Ali, F., Eid, M. R. & Sehaqui, R. Numerical analysis of the unsteady natural convection MHD Couette nanofluid flow in the presence of thermal radiation using single and two-phase nanofluid models for Cu–water nanofluids. *Int. J. Appl. Comput. Math.* **4**, 81 (2018).
32. Gholinia, M., Hoseini, M. & Gholinia, S. A numerical investigation of free convection MHD flow of Walters-B nanofluid over an inclined stretching sheet under the impact of Joule heating. *Therm. Sci. Eng. Prog.* **11**, 272–282 (2019).
33. Lahmar, S., Kezzar, M., Eid, M. R. & Sari, M. R. Heat transfer of squeezing unsteady nanofluid flow under the effects of an inclined magnetic field and variable thermal conductivity. *Phys. A Stat. Mech. Appl.* **540**, 123138 (2020).
34. Eid, M. R., Alsaedi, A., Muhammad, T. & Hayat, T. Comprehensive analysis of heat transfer of gold-blood nanofluid (Sisko-model) with thermal radiation. *Results Phys.* **7**, 4388–4393 (2017).
35. Eid, M. R. Time-dependent flow of water-NPs over a stretching sheet in a saturated porous medium in the stagnation-point region in the presence of chemical reaction. *J. Nanofluids* **6**, 550–557 (2017).
36. Kumar, K. G., Gireesha, B., Krishnamurthy, M. & Prasannakumara, B. Impact of convective condition on Marangoni convection flow and heat transfer in Casson nanofluid with uniform heat source sink. *J. Nanofluids* **7**, 108–114 (2018).
37. Kuznetsov, A. & Nield, D. Natural convective boundary-layer flow of a nanofluid past a vertical plate: a revised model. *Int. J. Therm. Sci.* **77**, 126–129 (2014).
38. Eid, M. R., Mahny, K. L., Muhammad, T. & Sheikholeslami, M. Numerical treatment for Carreau nanofluid flow over a porous nonlinear stretching surface. *Results Phys.* **8**, 1185–1193 (2018).
39. Eid, M. R. & Mahny, K. L. Flow and heat transfer in a porous medium saturated with a Sisko nanofluid over a nonlinearly stretching sheet with heat generation/absorption. *Heat Transf. Asian Res.* **47**, 54–71 (2018).
40. Muhammad, T. *et al.* Significance of Darcy–Forchheimer porous medium in nanofluid through carbon nanotubes. *Commun. Theor. Phys.* **70**, 361 (2018).
41. Jusoh, R., Nazar, R. & Pop, I. Three-dimensional flow of a nanofluid over a permeable stretching/shrinking surface with velocity slip: a revised model. *Phys. Fluids* **30**, 033604 (2018).
42. Al-Hossainy, A. F., Eid, M. R. & Zoromba, M. S. SQLM for external yield stress effect on 3D MHD nanofluid flow in a porous medium. *Phys. Scr.* **94**, 105208 (2019).
43. Boumaiza, N., Kezzar, M., Eid, M. R. & Tabet, I. On numerical and analytical solutions for mixed convection Falkner–Skan flow of nanofluids with variable thermal conductivity. *Waves Random Complex Media* <https://doi.org/10.1080/17455030.2019.1686550> (2019).
44. Eid, M. R., Mahny, K. L., Dar, A. & Muhammad, T. Numerical study for Carreau nanofluid flow over a convectively heated nonlinear stretching surface with chemically reactive species. *Phys. A Stat. Mech. Appl.* **540**, 123063 (2020).
45. Usman, M., Zubair, T., Hamid, M. & Haq, R. Novel modification in wavelets method to analyze unsteady flow of nanofluid between two infinitely parallel plates. *Chin. J. Phys.* **66**, 222–236 (2020).
46. Ibrahim, W. Magneto hydrodynamics (MHD) flow of a tangent hyperbolic fluid with nanoparticles past a stretching sheet with second order slip and convective boundary condition. *Results Phys.* **7**, 3723–3731 (2017).
47. Mahanthesh, B., Kumar, P. S., Gireesha, B., Manjunatha, S. & Gorla, R. Nonlinear convective and radiated flow of tangent hyperbolic liquid due to stretched surface with convective condition. *Results Phys.* **7**, 2404–2410 (2017).
48. Akbar, N. S., Nadeem, S., Haq, R. U. & Khan, Z. Numerical solutions of magnetohydrodynamic boundary layer flow of tangent hyperbolic fluid towards a stretching sheet. *Indian J. Phys.* **87**, 1121–1124 (2013).
49. Nadeem, S. & Shahzadi, I. Inspiration of induced magnetic field on nano hyperbolic tangent fluid in a curved channel. *AIP Adv.* **6**, 015110 (2016).
50. Nagendramma, V., Leelarathnam, A., Raju, C., Shehzad, S. & Hussain, T. Doubly stratified MHD tangent hyperbolic nanofluid flow due to permeable stretched cylinder. *Results Phys.* **9**, 23–32 (2018).
51. Oyelakin, I. S., Lalramneihmawii, P., Mondal, S., Nandy, S. K. & Sibanda, P. Thermophysical analysis of three-dimensional magnetohydrodynamic flow of a tangent hyperbolic nanofluid. *Eng. Rep.* **2**(4), e12144 (2020).
52. Salahuddin, T., Tanveer, A. & Malik, M. Homogeneous–heterogeneous reaction effects in flow of tangent hyperbolic fluid on a stretching cylinder. *Can. J. Phys.* **98**(2), 125–129 (2020).
53. Liao, S.-J. The proposed homotopy analysis technique for the solution of nonlinear problems, Ph.D. Thesis, Shanghai Jiao Tong University Shanghai, China (1992).

Author contributions

All authors contributed equally and looked over the final script and approved.

Competing interests

The authors declare no competing interests.

Additional information

Correspondence and requests for materials should be addressed to A.A.A. or M.R.E.

Reprints and permissions information is available at www.nature.com/reprints.

Publisher's note Springer Nature remains neutral with regard to jurisdictional claims in published maps and institutional affiliations.



Open Access This article is licensed under a Creative Commons Attribution 4.0 International License, which permits use, sharing, adaptation, distribution and reproduction in any medium or format, as long as you give appropriate credit to the original author(s) and the source, provide a link to the Creative Commons licence, and indicate if changes were made. The images or other third party material in this article are included in the article's Creative Commons licence, unless indicated otherwise in a credit line to the material. If material is not included in the article's Creative Commons licence and your intended use is not permitted by statutory regulation or exceeds the permitted use, you will need to obtain permission directly from the copyright holder. To view a copy of this licence, visit <http://creativecommons.org/licenses/by/4.0/>.

© The Author(s) 2020